

Fig. 3. Mark-Houwink-Sakurada plot for linear PSt standards and poly-5 obtained in THF at 30°C.

mined by PSt standards, whereas the M_r of the same sample is twice as high when determined by the "universal" calibration method that is heavily dependent on a homogeneous density distribution across the entire macromolecule. This discrepancy increases with M_r (Table 1, runs 2 to 4).

Self-condensing vinyl polymerization may be broadly applicable to a large number of polymerization techniques and different AB monomer structures. We have succeeded in applying it to the preparation of hyperbranched polymers by the "living" free radical polymerization (6) of AB vinyl monomers. The versatility of the approach stems from the variety of architectures that may be obtained with the use of several monomers such as styrene and substituted styrenes to produce unusual polymer architectures in one pot reactions. For example, stars and linear-dendritic hybrid structures can be obtained by sequential addition of appropriately selected monomers. Given the interesting properties of these hybrid structures (15, 16), a fast synthetic process for their preparation would be very beneficial.

REFERENCES AND NOTES

1. J. M. J. Fréchet, *Science* **263**, 1710 (1994); B. I. Voit, *Acta Polymer.* **46**, 87 (1995).
2. J. Issberner, R. Moors, F. Vögtle, *Angew. Chem. Int. Ed. Engl.* **33**, 2413 (1994); D. A. Tomalia and H. D. Durst, in *Top. Curr. Chem.* **165**, 193 (1993).
3. Y. H. Kim and O. W. Webster, *J. Am. Chem. Soc.* **112**, 4592 (1990).
4. L. J. Mathias and T. W. Carothers, *ibid.* **113**, 4043 (1991); C. J. Hawker, R. Lee, J. M. J. Fréchet, *ibid.*, p. 4583; V. Percec and M. Kawsumi, *Macromolecules* **25**, 3843 (1992); K. E. Uhrich, C. J. Hawker, J. M. J. Fréchet, S. R. Turner, *ibid.*, p. 4583; M. Suzuki, A. Ii, T. Saegusa, *ibid.*, p. 7071; E. Malmström, M. Johansson, A. Hult, *ibid.* **28**, 1698 (1995); M. Johansson, E. Malmström, A. Hult, *J. Polym. Sci. Polym. Chem. Ed.* **31**, 619 (1993).
5. S. R. Turner, B. I. Voit, T. H. Mourey, *Macromolecules* **26**, 4617 (1993).
6. D. H. Solomon, E. Rizzardo, P. Cacioli, U.S. Patent 4,581,429 (1986); M. K. Georges, R. P. N. Veregin, P. M. Kazmaier, G. K. Hamer, *Macromolecules* **26**, 2987 (1993); C. J. Hawker, *J. Am. Chem. Soc.* **116**, 11185 (1994); D. Mardare and K. Matyjaszewski, *Macromolecules* **27**, 645 (1994); M. Kato, M. Kami-

- gaito, M. Sawamoto, T. Higashimura, *ibid.* **28**, 1721 (1995).
7. Y. Ishihama, M. Sawamoto, T. Higashimura, *Polym. Bull.* **23**, 361 (1990); *ibid.* **24**, 201 (1990); *Macromolecules* **26**, 744 (1993).
 8. C.-H. Lin, J. S. Xiang, K. Matyjaszewski, *Macromolecules* **26**, 2785 (1993).
 9. G. A. Olah and S. J. Kuhn, U.S. Patent 3,024,291 (1962).
 10. A typical polymerization procedure is done as follows. Tetrabutylammonium bromide [TBAB, 0.748 g (2.3×10^{-3} mol)] was placed in a reaction flask equipped with a three-way stopcock in a dry box. A solution of SnCl_4 (0.68 ml, 5.8×10^{-3} mol) in 3.9 ml of dry methylene chloride was added by dried syringe under continuous flow of dry N_2 . The mixture was cooled to -20°C and a precooled solution of **1** (0.84 ml, 5.3×10^{-3} mol) in 5.2 ml of dry CH_2Cl_2 was added at once. After the addition, the reaction mixture turned transparently yellow, and its color changed to deep red during the polymerization. The polymerization system was quenched after 11 hours by addition of cold methanol (in excess to monomer). The reaction mixture was poured into 200 ml of CH_3OH to remove the remaining SnCl_4 and TBAB. The precipitate was filtered, dissolved in 50 ml of toluene, and washed three times with 2% aqueous solution of HCl and four times with distilled water. The organic layer was dried over MgSO_4 for several hours and concentrated. Toluene (10 ml) was then added and the solution was precipitated into 200 ml of CH_3OH . The polymer obtained was dried under dynamic vacuum at 50°C for 12 hours and subsequently analyzed by chromatographic and spectroscopic techniques. The polymers formed by this pro-

- cedure are soluble in toluene, tetrahydrofuran, and chlorinated solvents.
11. Because tetrabutylammonium bromide was used in these reactions, the equilibria are more complex (Br^- ions are also involved). However, Matyjaszewski and co-workers (8) have pointed out that the SnCl_4Br^- ions formed have a "similar effect on rates and polydispersities as [those produced from] tetrabutylammonium chloride" (p. 2790).
 12. L. Rique-Lurbet, M. Schappacher, A. Deffieux, *Macromolecules* **27**, 6318 (1994).
 13. It might be argued that possible heterogeneities in microstructure could affect data obtained across a single molecular weight distribution; therefore, our data were purposely taken with several samples, each of which yielded a data point representative of the entire sample.
 14. Universal calibration is not always applicable to the characterization of M_r in dendritic polymers because of its heavy dependence on homogeneous density distribution throughout the whole macromolecule. It is used here to emphasize the differences in the solution behavior of the self-condensed vinyl polymers as compared with closely related, but linear, polymers.
 15. I. Gitsov and J. M. J. Fréchet, *Macromolecules* **26**, 6536 (1993); *ibid.* **27**, 7309 (1994).
 16. T. M. Chapman, G. L. Hillyer, E. J. Mahan, K. A. Shaffer, *J. Am. Chem. Soc.* **116**, 11195 (1994).
 17. Financial support of this research by the National Science Foundation (DMR-92244210) and analytical support by the Polymer Characterization Facility of the Cornell Materials Science Center (NSF DMR-9121654) is acknowledged with thanks.

18 April 1995; accepted 21 June 1995

Scanning Interferometric Apertureless Microscopy: Optical Imaging at 10 Angstrom Resolution

F. Zenhausern, Y. Martin, H. K. Wickramasinghe*

Interferometric near-field optical microscopy achieving a resolution of 10 angstroms is demonstrated. The scattered electric field variation caused by a vibrating probe tip in close proximity to a sample surface is measured by encoding it as a modulation in the optical phase of one arm of an interferometer. Unlike in regular near-field optical microscopes, where the contrast results from a weak source (or aperture) dipole interacting with the polarizability of the sample, the present form of imaging relies on a fundamentally different contrast mechanism: sensing the dipole-dipole coupling of two externally driven dipoles (the tip and sample dipoles) as their spacing is modulated.

Near-field scanning microscopy at microwave frequencies (1) and its extension to the visible region [near-field scanning optical microscopy (NSOM)] (2, 3) at resolutions under 50 nm have attracted much attention (4–7). Recently, a scanning interferometric apertureless microscope (SIAM) was introduced (8, 9) with which one can measure the scattered electric-field variation caused by a vibrating and scanning probe tip in close proximity to a sample surface by encoding it as a modulation in the phase of one arm of an interferometer. Here, SIAM images of various samples are presented at a re-

solution of 1 nm, almost two orders of magnitude superior to that of other NSOM images. A basic theory based on coupled dipoles is put forward and compared with experiments. It shows that the contrast mechanisms are fundamentally different from those in regular near-field optical microscopes because of a unique dipole-dipole coupling mechanism. Furthermore, the theory predicts the ability to measure complex susceptibility down to the atomic level.

Experiments were performed in the transmission mode (9). An incident laser beam is focused on the back surface of a transparent substrate holding the sample (Fig. 1). A tip vibrating in the z direction (frequency $f_z = 250$ kHz, spring constant = 20 N/m, tip-end diameter ≈ 5 nm, vibra-

IBM Research Division, T. J. Watson Research Center, Post Office Box 218, Yorktown Heights, NY 10598, USA.

*To whom correspondence should be addressed.

tion amplitude = 6 to 10 nm) is brought close to the focused spot and stabilized at 1 to 2 nm over the sample surface with an attractive-mode atomic force microscope (AFM) (10). The return beam $E_r' + E_s$ (reflection from substrate of the plus tip-sample scattering) is detected with an interferometer by combining it with a reference beam E_r . The output signal of the interferometer measures either the amplitude of $(E_r' + E_s)$ or its phase difference with E_r , which represents the contrast mechanisms.

An AFM image of a cleaved mica surface (Fig. 2A) shows a 0.25-nm monatomic terrace on the left that appears as a bright scattering region in the simultaneously recorded optical image (Fig. 2B). The AFM image also shows a step in the center composed of about 15 atomic layers. The optical image shows the same feature as a bright band across its center but in addition shows much sharper detail (see arrows) not visible in the AFM image. These features could be subsurface defects in the mica as they do not appear in the topography; the smallest discernible feature size visible optically is approximately 1 nm and corresponds to an interferometric phase shift of 2×10^{-5} radian.

In the next experiment (Fig. 3), index-matching oil was dispersed into tiny droplets on cleaved mica by repeatedly scanning an AFM tip across its surface (for about 1 hour at a force gradient of 0.1 N/m). The data were acquired at a force gradient an order of magnitude lower, and AFM and optical images were recorded simultaneously. The AFM topography image (Fig. 3A), which represents constant-force gradient contours,

shows the oil droplets as bumps on the mica surface. Certain regions also show dips (top right arrow); these dips indicate that some oil droplets are probably charged and therefore locally reduce the overall force gradient on the tip caused by electrostatic interactions. The optical image (Fig. 3B) shows the oil droplets as enhanced scattering centers; the dips in the AFM image show up as optically bright regions with no sensitivity to charge. Note that a feature in the AFM image (top left arrow) is totally absent in the optical image. One can characterize this topographic feature, which produces little scattering and shows optical properties, as quite different from the oil droplets. The smallest feature resolved optically (bottom right arrow in Fig. 3A) is about 1 nm across, as in the earlier experiments, and a phase change of 10^{-4} radian is measured.

Experiments have indicated that in some situations the image contrast can switch, depending on the optical parameters at the tip end, from high contrast to low contrast or inverted contrast. A test sample was prepared by spinning 45-nm fluorescent polystyrene spheres (11) on a cleaved mica

surface. Figure 4A shows the AFM image of an island of polystyrene spheres, the topography showing individual spheres. Figure 4B shows the simultaneously recorded optical image, with interferometric phase modulation of about 10^{-3} radian. A sudden change appears in the optical image, whereas the AFM image shows virtually no change (on careful examination of AFM line scans, a minute change in the tip z position of about 5 nm is detected). This can be explained if the tip picked up a particle as it raster scanned the sample, perhaps a fluorescent dye molecule, which changed the phase of the scattered field. In the top region of Fig. 4B, the spheres appear as a low signal in a bright background; here the scattered electric field E_s is expected to have a component $\pi/2$ out of phase with E_r' . In the lower region, the contrast is weaker but reversed, which implies that E_s has a component π out of phase as compared with the top region. Several similar results demonstrate that small particles (around 5 nm) can significantly affect the scattered field and reveal the high sensitivity of the SIAM technique to small changes in the tip-sample

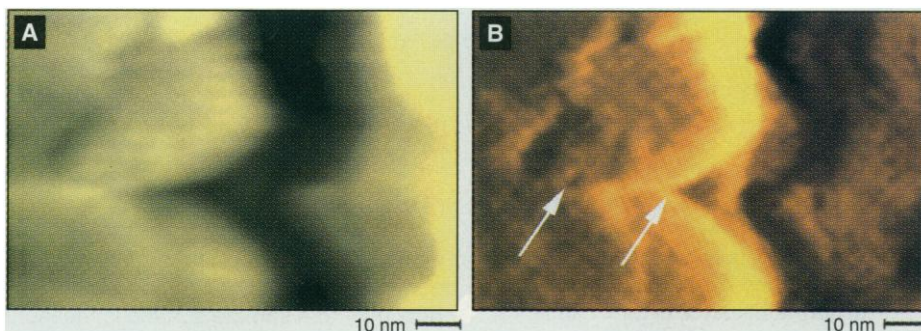


Fig. 2. (A) Attractive-mode AFM image showing atomic terraces on the mica. (B) Simultaneously recorded SIAM image revealing bright scattering regions corresponding to the atomic terraces but also showing fine subsurface features not present in the AFM image (indicated by arrows); smallest resolvable feature ≈ 1 nm.

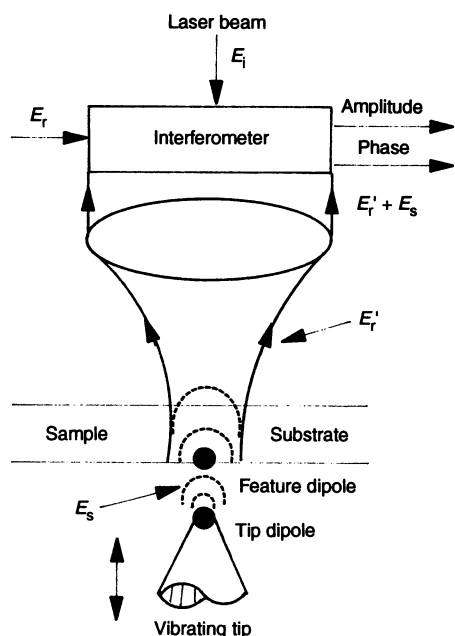


Fig. 1. Principle of the SIAM method.

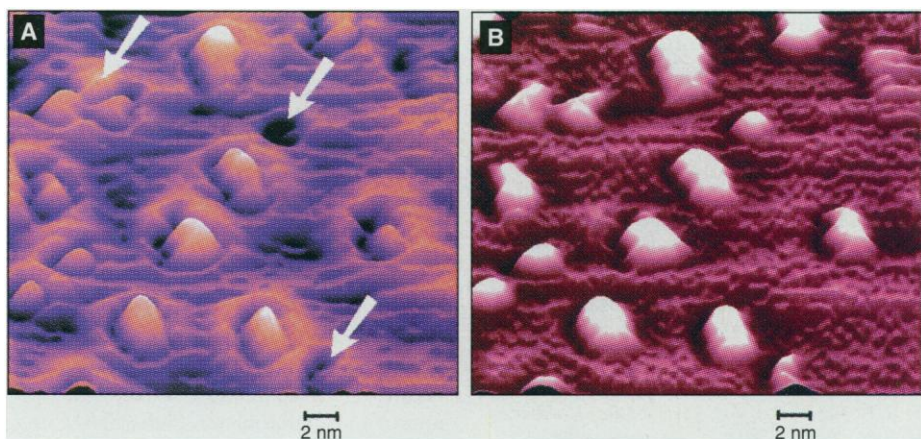


Fig. 3. Dispersed oil droplets on mica. (A) Attractive-mode AFM topography image showing most droplets as bumps in the image, although some are shown as dips because of electrostatic charging effects. (B) Simultaneously recorded optical image showing the oil droplets as bright scattering regions. Some features in the AFM image are absent in the optical image and others are inverted in contrast (arrows); smallest resolvable feature ≈ 1 nm.

optical interaction. As further evidence for the source of contrast, a 100-nm chromium grating was scanned at constant height with the AFM to remove any tip-height related signal. Although no detail was visible in the AFM image, the optical image showed strong contrast at heights of about 10 nm or less as a result of dipole-dipole coupling.

A theory based on coupled dipoles can be derived to understand the contrast mecha-

nism in SIAM. Because the optical dipole interaction varies with the tip-feature spacing (r) as r^{-3} , the measured signal primarily derives from the tip end. One can therefore model the tip and the sample features as spheres of radius a (Fig. 1), with polarizabilities α_t and α_f , immersed in a driving electric field E_i . The equation (12) that describes the polarizability modulation $\Delta\alpha$ resulting from the coupling between the tip and feature is

$$\Delta\alpha = \frac{2\alpha_t\alpha_f}{(r^2 + a^2)^{3/2}} \quad (1)$$

The modulation ΔE_s of the scattered field E_s caused by the polarizability modulation $\Delta\alpha$ can be calculated by applying a scattering matrix (S) treatment for small particles (13). The spherically scattered wave at a distance d in the far field is given by

$$E_s = \frac{E_i}{ikd}(S); \quad \Delta E_s = \frac{E_i}{ikd}(\Delta S) \quad (2)$$

For particles significantly smaller than 50 nm, where $ka \ll 1$ ($k = 2\pi n/\lambda$ being the optical propagation constant of a signal of wavelength λ in a medium of refractive index n), the relevant scattering matrix component S (which has both real and imaginary components) can be written in terms of the polarizability α

$$S = ik^3\alpha; \quad \Delta S = ik^3\Delta\alpha \quad (3)$$

where higher order terms in k and α are neglected.

The scattered electric-field modulation ΔE_s is directly proportional to $\Delta\alpha$; one therefore expects to see a strong decrease in ΔE_s as the tip-feature dipole-dipole coupling decreases with increasing r . Figure 5 gives a plot of the optical signal as a function of spacing, compared with the theoretical curve obtained from Eq. 1. The sample was a chromium film, acting as a mirror, and the dipole-dipole interaction consisted of the tip interacting with its image. We observed a strong decrease in the optical signal over a distance corresponding to the tip diameter, 370 Å in this case. Furthermore, Eq. 1 shows that $\Delta\alpha$ is proportional to the product of α_t and α_f . Consequently, the phase of ΔE_s can change drastically depending on the complex polarizability of the tip end, as observed in Fig. 4.

In general, the scattered field will have a component $E_{s\phi}$ orthogonal in phase to E_r that provides a phase shift and a component E_{se} out of phase with E_r that provides an extinction in the interferometer. Combining Eqs. 1 and 2 with the far-field expression for E_r , $E_r = E_i\lambda n/5\pi idNA^2$ (9), where NA is the numerical aperture, and noting that the polarizability is related to the susceptibility χ by

$$\alpha = \frac{\chi}{4\pi} \left(\frac{4}{3} \pi a^3 \right) \quad (4)$$

expressions for the phase shift and extinction modulation in the interferometer are

$$\frac{\Delta E_{se}}{E_r} = \frac{5}{9} (ka)^3 \frac{NA^2}{n^2} \text{Im}(\chi_t\chi_f) \quad (5)$$

$$\frac{\Delta E_{s\phi}}{E_r} = \frac{5}{9} (ka)^3 \frac{NA^2}{n^2} \text{Re}(\chi_t\chi_f) \quad (6)$$

Several conclusions can be inferred from these equations. First, both the real and imaginary parts of the susceptibility of a feature can be determined—in principle, down to the atomic (9) scale—with two simultaneous measurements of in-phase and quadrature components, tip susceptibility being measured independently with the use of a known reference surface as the sample. Experimentally, absolute values of interferometric signals and their variation with tip susceptibility (a factor of 4 increase for an Al tip versus Si) agree with Eqs. 5 and 6.

Another key advantage of the interferometric measurement in SIAM is the detection of the scattered electric fields, which vary as $(ka)^3$, rather than intensities, which vary as $(ka)^6$, as in typical near-field optical systems. The interferometric signal is significantly higher than background noise (from sources such as stray light, dark current, or thermal noise), which is inevitably present in experimental setups. By contrast, this background noise severely limits the sensitivity of typical NSOM at high resolution (smaller than 50 nm). The understanding of the principles involved in SIAM opens up many capabilities for imaging and spectroscopy at subnanometer scales and particularly extends its application to biology.

REFERENCES AND NOTES

1. E. A. Ash and G. Nicholls, *Nature* **237**, 510 (1972).
2. D. W. Pohl, W. Denk, M. Lanz, *Appl. Phys. Lett.* **44**, 651 (1984).
3. A. Lewis, M. Issacson, A. Haratounian, A. Murray, *Ultramicroscopy* **13**, 227 (1984).
4. M. Fee, S. Chu, T. W. Haensch, *Opt. Commun.* **69**, 219 (1989).
5. E. Betzig and J. K. Trautman, *Science* **257**, 189 (1992).
6. R. Toledo-Crow, P. C. Yang, Y. Chen, M. Vaez-Iravani, *Appl. Phys. Lett.* **60**, 2957 (1992).
7. E. Betzig and R. J. Chichester, *Science* **262**, 1422 (1993).
8. H. K. Wickramasinghe and C. C. Williams, U.S. Patent 4 947 034 (28 April 1989); IBM Disclosure Y0887-0949 (December 1987).
9. F. Zenhausern, M. P. O'Boyle, H. K. Wickramasinghe, *Appl. Phys. Lett.* **65**, 1623 (1994).
10. Y. Martin, C. C. Williams, H. K. Wickramasinghe, *J. Appl. Phys.* **61**, 4723 (1987).
11. The fluorescein isothiocyanate latex spheres were provided by Polysciences, lot #17151.
12. J. D. Jackson, *Classical Electrodynamics* (Wiley, New York, 1957).
13. H. C. van de Hulst, *Light Scattering by Small Particles* (Wiley, New York, 1957).
14. F.Z. was supported by the Swiss National Foundation grant 5002-36851.

27 April 1995; accepted 6 July 1995

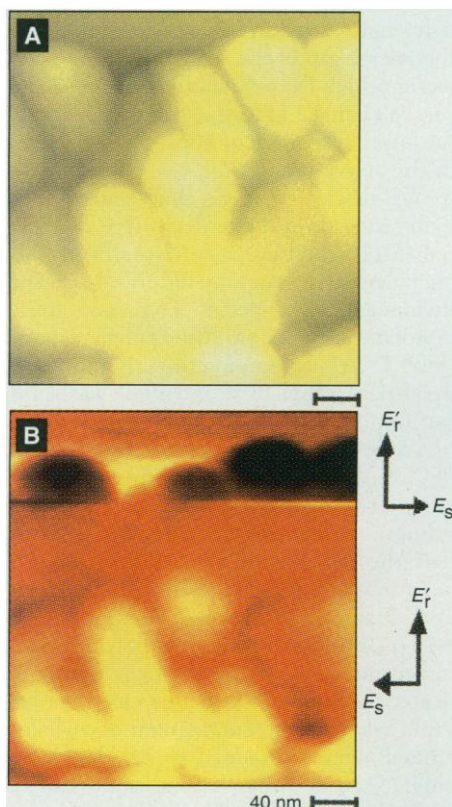


Fig. 4. Images of 45-nm fluorescent polystyrene spheres on mica. (A) Attractive-mode AFM topography. (B) Simultaneously recorded SIAM image showing contrast reversals in different regions caused by a small particle (≈ 5 nm) sticking to the tip.

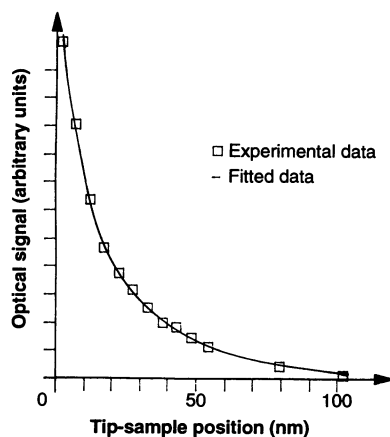


Fig. 5. Measured optical dipole-coupling signal (after subtraction of instrument response) versus tip-sample spacing, compared with theory (Eq. 1).